IMAGING

An optical nanoreporter of endolysosomal lipid accumulation reveals enduring effects of diet on hepatic macrophages in vivo

Thomas V. Galassi^{1,2}, Prakrit V. Jena¹, Janki Shah¹, Geyou Ao³, Elizabeth Molitor⁴, Yaron Bram², Angela Frankel², Jiwoon Park², Jose Jessurun², Daniel S. Ory⁴, Adriana Haimovitz-Friedman¹, Daniel Roxbury⁵, Jeetain Mittal⁶, Ming Zheng³, Robert E. Schwartz², Daniel A. Heller^{1,2}*

The abnormal accumulation of lipids within the endolysosomal lumen occurs in many conditions, including lysosomal storage disorders, atherosclerosis, nonalcoholic fatty liver disease (NAFLD), and drug-induced phospholipidosis. Current methods cannot monitor endolysosomal lipid content in vivo, hindering preclinical drug development and research into the mechanisms linking endolysosomal lipid accumulation to disease progression. We developed a single-walled carbon nanotube-based optical reporter that noninvasively measures endolysosomal lipid accumulation via bandgap modulation of its intrinsic near-infrared emission. The reporter detected lipid accumulation in Niemann-Pick disease, atherosclerosis, and NAFLD models in vivo. By applying the reporter to the study of NAFLD, we found that elevated lipid quantities in hepatic macrophages caused by a high-fat diet persist long after reverting to a normal diet. The reporter dynamically monitored endolysosomal lipid accumulation in vivo over time scales ranging from minutes to weeks, indicating its potential to accelerate preclinical research and drug development processes.

Copyright © 2018
The Authors, some rights reserved; exclusive licensee
American Association for the Advancement of Science. No claim to original U.S.
Government Works

INTRODUCTION

The accumulation of lipids in endolysosomal organelles has been implicated in diverse pathologies including neurodegenerative diseases (1), lysosomal storage disorders (2), atherosclerosis (3), nonalcoholic fatty liver disease (NAFLD) (3), and drug-induced phospholipidosis (DIPL) (4). However, current methods for the in vivo detection of endolysosomal lipid accumulation are lacking. Although techniques such as magnetic resonance imaging, magnetic resonance spectroscopy, positron emission topography, computer tomography, nuclear magnetic resonance spectroscopy, ultrasound, and dual-energy x-ray absorptiometry have been effectively used in the clinic to quantify lipid content in specific organs or tissues, they show no specificity for individual organelles (5). Similarly, optical coherence tomography (6) and intracoronary near-infrared (NIR) spectroscopy (7) can detect lipid-rich atherosclerotic plaques in vivo, but these methods also do not provide information on the lipid content of specific organelles. Transmission electron microscopy (TEM), currently the gold standard for the detection of endolysosomal lipid accumulation present in preclinical animal models (8), is expensive, low throughput, and only applicable for resected tissues and gives qualitative and subjective results (9). Experimental probes with the ability to rapidly and noninvasively monitor lipid flux or accumulation in endolysosomal organelles in in vivo animal models do not currently exist.

A noninvasive method to detect endolysosomal lipid accumulation in vivo would have broad applications and facilitate preclinical research and drug development. In the context of lysosomal storage disorders, such a method would allow for the in vivo efficacy of candidate compounds to be assessed rapidly and noninvasively in animal

¹Memorial Sloan Kettering Cancer Center, New York, NY 10065, USA. ²Weill Cornell Medicine, New York, NY 10065, USA. ³National Institute of Standards and Technology, Gaithersburg, MD 20899, USA. ⁴Department of Medicine, Washington University School of Medicine, St. Louis, MO 63110, USA. ⁵Department of Chemical Engineering, University of Rhode Island, Kingston, RI 02881, USA ⁶Department of Chemical and Biomolecular Engineering, Lehigh University, Bethlehem, PA 18015, USA. *Corresponding author. Email: hellerd@mskcc.org

models, rather than via long-term survival studies or tissue-based histological end points. Such a method could be directly applied to the assessment of DIPL, a condition caused by more than 350 drug candidates and marketed drugs (10). DIPL is characterized by the accumulation of drug, phospholipid, and cholesterol in the lysosomal lumen of cells (4, 10) and has been recognized by the U.S. Food and Drug Administration as a major regulatory concern that impedes the drug development process (4, 11, 12). When assessing candidate compounds, pharmaceutical companies frequently assess DIPL in vivo, with TEM serving as the gold standard of detection methods (10). A technique that quantitatively, rapidly, and noninvasively assesses endolysosomal lipid accumulation in vivo could replace TEM measurements in the identification of DIPL, streamlining the drug development process.

In addition to drug development, a noninvasive and rapid method to detect endolysosomal lipid accumulation in vivo would also aid in the investigation of disease pathogenesis. In the study of NAFLD, a spectrum of disorders affecting more than 30% of the general population (13), past work suggests that the accumulation of endolysosomal lipids in Kupffer cells (KCs), the resident liver macrophages, may be implicated in disease progression toward nonalcoholic steatohepatitis (NASH) (14, 15). NASH is a progressive form of NAFLD that is characterized by the concurrent presence of hepatic steatosis and inflammation and may lead to fibrosis, cirrhosis, or hepatocellular carcinoma (13, 16). Despite the negative health effects associated with the progression of early-stage NAFLD to NASH, the underlying mechanisms remain poorly understood, and the relationship between KC endolysosomal lipid accumulation and disease progression has not been extensively studied. This is due, in part, to a lack of methods to monitor KC endolysosomal lipid flux or accumulation in live animals. Such a method would serve as a valuable tool in the elucidation of NAFLD/NASH pathogenesis and would aid in the development of new therapies.

Here, we present an optical reporter that noninvasively monitors endolysosomal lipid accumulation and flux from within KCs in vivo. The reporter localizes within endolysosomal organelles rapidly upon intravenous injection and can be monitored noninvasively via NIR excitation/emission. We detected hepatic lipid accumulation in animal models of the lysosomal lipid storage diseases Niemann-Pick disease type A/B (NPA/B) and Niemann-Pick disease type C (NPC) and used the reporter to monitor the accumulation of lipids in KC endolysosomal organelles and the effects of dietary intervention in mouse models of NAFLD and NASH.

RESULTS

Reporter development and characterization

To develop an in vivo reporter of KC endolysosomal lipid accumulation, we used the intrinsic NIR fluorescence from a single-walled carbon nanotube (SWCNT) that was noncovalently complexed with single-stranded (ss) DNA (DNA-SWCNT). This builds on past work by our group, demonstrating that DNA-SWCNTs localize to endolysosomal organelles, where they can detect lipid accumulation in vitro without adversely affecting organelle size, shape, integrity, capacity to digest lipoproteins, cell viability, or proliferation (17).

A population of SWCNTs contains discrete structural species (chiralities) that differ in diameter and chiral angle (18). These discrete chiralities are identified by the chiral integers (n,m) (18), and semiconducting SWCNT chiralities are intrinsically photoluminescent in the NIR region of the spectrum (19). We initially assessed the potential of several DNA-sequence nanotube chirality combinations to serve as a reporter of endolysosomal lipid accumulation (fig. S1). In solution, each of the tested combinations exhibited a >9-nm decrease in emission center wavelength in response to low-density lipoprotein (LDL; 0.5 mg/ml; fig. S2A). When internalized by cells exhibiting endolvsosomal lipid accumulation, each tested combination once again exhibited a decrease in emission center wavelength compared with untreated controls, and ssCTTC₃TTC-(9,4) showed the greatest emission response (8.3 nm; fig. S2B). The emission wavelength of ssCTTC₃TTC-(9,4) was minimally affected by a decrease in pH, highlighting its potential as a reporter of lipid accumulation in the acidic endolysosomal organelles in vivo (fig. S3).

Building off of the previously developed reporter for endolyso-somal lipid accumulation in vitro (17), the ssCTTC₃TTC-(9,4) construct is a second-generation nanomaterial engineered for in vivo applications. It is purified through an aqueous two-phase (ATP) polymer separation method (20) rather than through ion-exchange high-performance liquid chromatography (IEX-HPLC) (21), which was used to purify the in vitro reporter (17). Unlike IEX-HPLC, the ATP separation method is an inexpensive, highly scalable process that allows for the production of the quantities of structurally sorted SWCNT needed for thorough in vivo studies with multiple biological replicates (22). This second-generation reporter has an emission wavelength of ~1125 nm, away from the lipid absorption band at ~1210 nm (23), which should facilitate in vivo measurements (23, 24).

After identifying ssCTTC₃TTC-(9,4) as a potential reporter of endolysosomal lipid accumulation in vivo, we characterized its optical response in a biologically relevant environment in vitro. After acquiring a protein corona via incubation in cell culture medium with 1% fetal bovine serum (FBS) for 90 min, the reporter had an excitation maximum at 732 nm (essentially on resonance with the 730-nm laser excitation used) and an emission maximum at 1128 nm (Fig. 1A). When exposed to various classes of biomolecules and water-soluble lipid analogs, the reporter showed minimal response

to near-saturating concentrations of bovine serum albumin (BSA), genomic DNA, and carboxymethylcellulose (CMC) but exhibited an ~6- to 8-nm decrease in emission center wavelength (herein described as a "blue shift") in response to the water-soluble lipid analogs polyethylene glycol (PEG)–cholesterol, methoxy PEG (mPEG)–ceramide (C16), and mPEG-phosphoethanolamine (18:0) (Fig. 1B and fig. S4). The median length of the reporter as measured via atomic force microscopy was 133 nm (fig. S5).

To better understand the reporter's mechanism of detection, we conducted all-atom replica exchange molecular dynamics simulations. Consistent with our previous study (17), simulations suggested that sphingomyelin or cholesterol molecules bind to the reporter surface via hydrophobic interactions, decreasing the water density in the nanotube's immediate vicinity (Fig. 1, C and D, and figs. S6 and S7). This likely leads to an effective decrease of the local solvent dielectric, resulting in the observed blue shift (17).

Reporter validation in live cells

After in silico and in vitro characterization of the reporter, we validated its functionality in live cells. Endolysosomal lipid accumulation was induced in RAW 264.7 macrophages via three distinct mechanisms: Cells were treated with U18666A to mimic the lysosomal storage disorder NPC by inhibiting the NPC1 protein (25), which causes the accumulation of unesterified cholesterol in lysosomes (26); cells were treated with Lalistat 3a2, which inhibits the enzyme lysosomal acid lipase (LAL) (27) and causes a phenotype similar to that seen in Wolman's disease, where LAL deficiency causes an accumulation of esterified cholesterol in lysosomes (28); or cells were treated with imipramine hydrochloride, which inhibits the enzyme acid sphingomyelinase, causing the accumulation of sphingomyelin in lysosomes similar to what is seen in NPA/B disease (29). After treatment with each inhibitor, the reporter was incubated with cells as previously described (17). Histograms obtained from NIR hyperspectral microscopy (30) of the reporter from within cells showed a single blue-shifted population under all three drug treatments (Fig. 1, E and F), and a mean emission center wavelength that was ~6 nm blue-shifted compared to emission from untreated control cells (figs. S8 and S9), demonstrating the ability of ssCTTC₃TTC-(9,4) to detect endolysosomal lipid accumulation in live cells. Moreover, the reporter red-shifted in response to the removal of lipids from endolysosomal organelles via treatment with 2-(hydroxypropyl)-β-cyclodextrin (fig. S10) (31), suggesting reversibility. The reporter did not affect the ability of cells to hydrolyze lipoproteins (fig. S11).

Reporter biodistribution in vivo

After validating the reporter's ability to detect endolysosomal lipid accumulation in vitro, we investigated its biodistribution in vivo by intravenous injection. "Unprotected" nanoparticles are known to be opsonized and rapidly removed from the bloodstream by the macrophages of the reticuloendothelial system after intravenous injection, resulting in the accumulation of nanoparticles in the liver and spleen (32–35). Partially protecting SWCNTs from opsonization via noncovalent functionalization with PEGylated polymers still leads to accumulation in these organs and localization to resident macrophages (36–38). We saw similar results with the ssCTTC₃TTC nanotubes, as kinetic measurements of reporter fluorescence in vivo showed an increase in fluorescence intensity measured from all regions of the mouse immediately after injection, which was followed

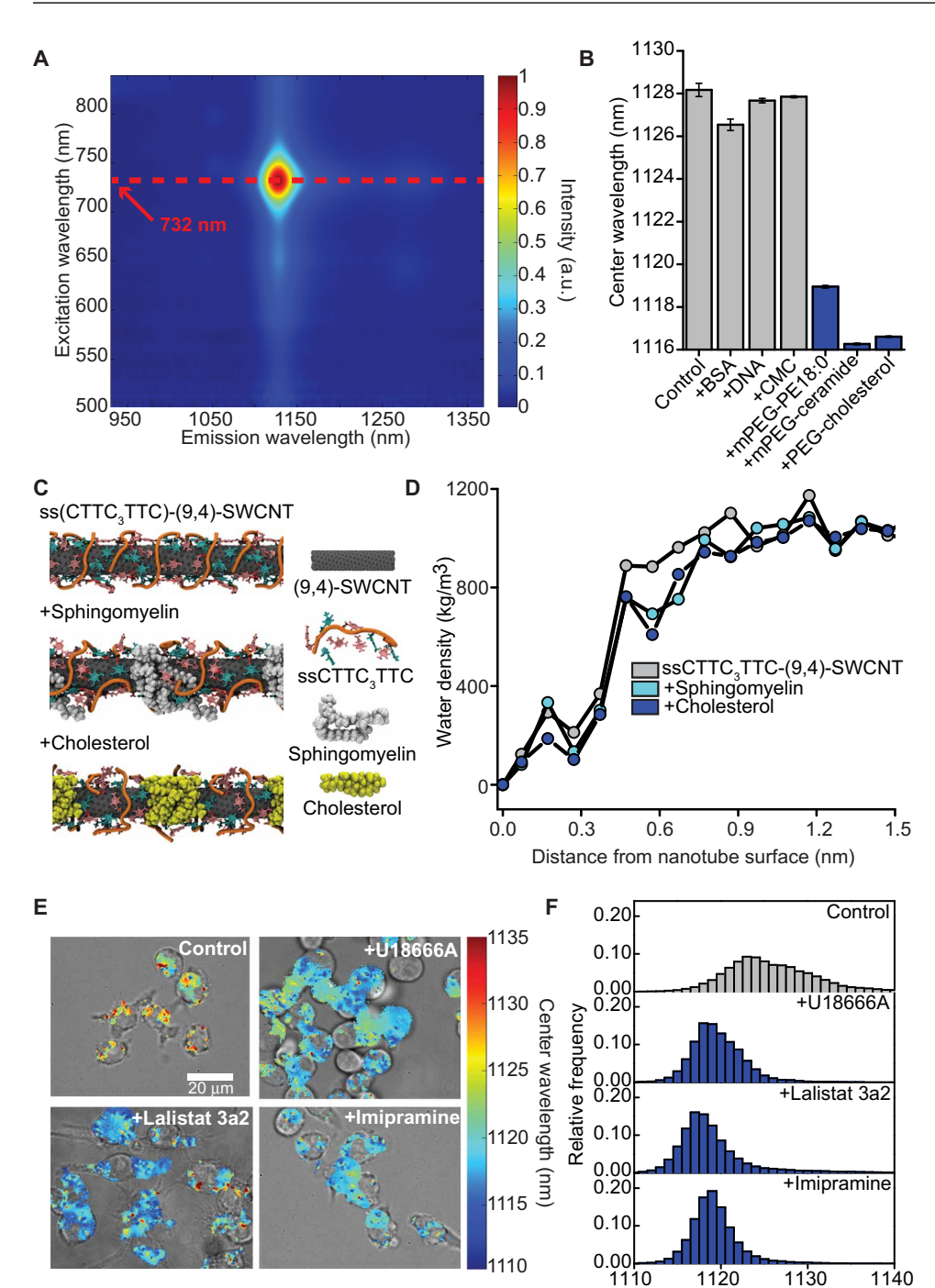


Fig. 1. Characterization of the ssCTTC₃TTC-(9,4) optical reporter. (**A**) Photoluminescence excitation emission plot of ssCTTC₃TTC-(9,4). a.u., arbitrary units. (**B**) Nanotube emission center wavelength \pm SD in cell culture medium with 1% FBS at near-saturating concentrations of BSA (20 mg/ml), salmon testes double-stranded DNA (1 mg/ml), CMC (5 mg/ml), mPEG-phosphoethanolamine 18:0 (mPEG-PE 18:0; 5.93 mM), PEG-cholesterol (5.93 mM), or mPEG-ceramide (5.93 mM). Error bars represent SD from n=3 technical replicates. (**C**) Frames from molecular dynamics simulations showing equilibrated structures of the ssCTTC₃TTC-(9,4) nanotube complex in the presence of cholesterol and sphingomyelin. (**D**) Water density as a function of distance from the surface of ssCTTC₃TTC-(9,4) nanotube complexes, in the presence of sphingomyelin or cholesterol, or with no lipids present. (**E**) Overlays of transmitted light and NIR hyperspectral images of the reporter in RAW 264.7 macrophages cultured in complete cell culture medium with or without U18666A (3 µg/ml), Lalistat 3a2 (10 µM), or imipramine hydrochloride (10 µM). (**F**) Histogram of emission center wavelengths from all pixels with NIR emission from the NIR hyperspectral images of cells under the conditions described in (E).

Center wavelength (nm)

by rapid decrease in all regions of the mouse with the exception of the area containing the liver (Fig. 2A). Over the next 6 hours, the fluorescence signal in the liver region decreased, potentially due to SWCNT being trafficked from the liver vasculature into KC lysosomes. The signal was then relatively stable from 24 to 72 hours after injection, although it decreased slightly over that time frame (Fig. 2A). These results suggest rapid clearance of ssCTTC₃TTC-encapsulated carbon nanotubes from blood and retention in the liver region, even after 72 hours (Fig. 2A). NIR images acquired in vivo after 24 hours (Fig. 2B) and ex vivo imaging of the extracted organs (Fig. 2, C and D) confirmed the specific localization of the reporter to the liver, with negligible NIR emission from other organs. NIR hyperspectral imaging of isolated hepatic cells confirmed nanotube uptake by KCs, consistent with the typical behavior of the mononuclear phagocyte system (Fig. 2E and Supplementary Materials and Methods) (34). Together, these data demonstrate the potential of the reporter to assess KC endolysosomal lipid accumulation or flux in a live animal.

Noninvasive detection of lysosomal storage disorders in vivo

The ability of the reporter to noninvasively detect endolysosomal lipid accumulation in KCs in vivo was tested using an acid sphingomyelinase knockout (ASMKO) (39) and an NPC1 I1061T (Npc^{tm(I1061T)Ďso}) knock-in mouse model (40). These mouse lines model NPA/B and NPC disease, respectively, and accumulate lipids within the endolysosomal organelles of many cell types, including KCs. To determine whether ssCTTC₃TTC-(9,4) could detect this accumulation, the reporter was injected intravenously into mice, and after 24 hours, reporter emission from the liver was obtained using a NIR in vivo spectroscope (fig. S12) (41). The in vivo spectra showed a high signal-to-noise ratio of more than 14.64 ± 5.18 , with distinct blue shifts of ~4.2 and ~5.3 nm in ASMKO and Npc^{tm(I1061T)Dso} mice, respectively, compared to age-matched wild-type controls (Fig. 3). The difference in reporter emission was maintained ex vivo (Fig. 3) and in frozen resected liver tissues (Fig. 3 and tables S1 and S2). The phenotype of each mouse was confirmed

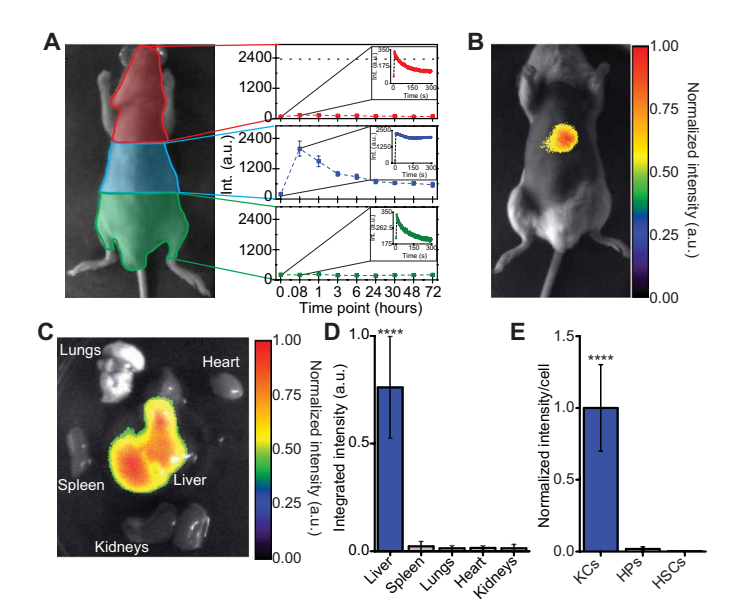


Fig. 2. Reporter biodistribution. (**A**) Quantification of fluorescence over time in different regions of mice after intravenous injection of $ssCTTC_3TTC-SWCNT$. Results are averaged for five mice, and error bars represent SD. Insets represent the average fluorescence intensity (Int.) in the specified region immediately after injection. Error bars have been removed for clarity. (**B**) Fluorescence image of the reporter in vivo in a mouse, 24 hours after intravenous injection (200 ng). (**C**) Fluorescence image of the reporter in mouse organs ex vivo, 24 hours after injection as in (B). (**D**) Quantification of $ssCTTC_3TTC-SWCNT$ emission spectra ex vivo obtained with a NIR spectroscope. ****P < 0.0001 versus other groups, one-way analysis of variance (ANOVA) with Dunnett's post-test. Error bars represent SD. n=3 mice per group. (**E**) Quantification of $ssCTTC_3TTC-SWCNT$ emission in isolated murine KCs, hepatocytes (HPs), and hepatic stellate cells (HSCs), 24 hours after intravenous injection. *****P < 0.001, one-way ANOVA with Tukey's post-test. Error bars represent SEM. n=49 to 62 cells per group.

via histology, which showed lipid-laden KCs and hepatocytes (figs. S13 to S18).

Dynamic detection of oxidized LDL accumulation

We next investigated the ability of the reporter to detect the uptake and endolysosomal accumulation of oxidized LDL (oxLDL), a process that has been implicated in the development of atherosclerosis and NASH. oxLDL was injected intravenously in mice 24 hours after the injection of the reporter to ensure that any interaction between oxLDL and the reporter occurred in endolysosomal organelles rather than in the circulation (Fig. 4A). Six hours after oxLDL injection, reporter emission from KCs of injected mice was measured noninvasively and displayed monotonic blue shifting as the injected dose was increased, with a limit of detection between 2 and 20 μg (Fig. 4B). By repeatedly measuring reporter emission at different time points just before, and after, oxLDL injection, we quantified the kinetics of oxLDL uptake and endolysosomal accumulation by KCs (Fig. 4C). When 200 µg of oxLDL was injected, accumulation could be detected dynamically within 30 min, and a single exponential fit found that the average time constant for this process was 60.63 min (Fig. 4D and fig. S19). Ex vivo testing of the reporter in whole blood samples with varying concentrations of total cholesterol revealed no significant correlation between reporter emission and cholesterol concentration, indicating that reporter measurements were not compromised because of the interference of lipids/lipoproteins

circulating in the bloodstream (fig. S20). This confirmed the ability of the reporter to dynamically detect the uptake and accumulation of oxLDL into KCs in vivo.

Monitoring KC endolysosomal lipids in a NAFLD model

Using the reporter, we examined the relationship between KC endolysosomal lipid accumulation and NAFLD progression toward NASH. Male C57BL/6 mice were fed standard chow (SC) or a Western diet (WD) (42% calories from fat) with water supplemented with high-fructose corn syrup (HFCS) equivalent for 1 to 3 months. When administered more than 22 to 52 weeks, this model is known to lead to the development of steatosis, fibrosis, inflammation, and hepatocyte ballooning, recapitulating human NASH (42, 43). Moreover, male C57BL/6 mice fed the WD for 20 months have been shown to develop all of the conditions described above as well as dysplastic hepatic tumors, thus displaying all major NAFLD/NASH sequelae (43). By administering this diet for shorter periods, we aimed to investigate KC endolysosomal lipid accumulation in an early stage of a progressive model of NAFLD.

As expected, after 3 months of the WD and HFCS, mice developed obesity (fig. S21). Histological sections of livers from WD-fed mice indicated an increase in hepatic steatosis over time (Fig. 5A), an observation that was confirmed by a trained pathologist and through the quantification of steatotic area in hematoxylin and eosin (H&E) sections (Fig. 5B). Hepatic sections stained with CK8/18 and F4/80 showed lipid accumulation in both hepatocytes and KCs at 1 and 3 months of WD feeding (figs. S22 to S25). Moreover, H&E-stained tissue sections showed inflammatory foci (as observed by a trained pathologist) in all but one mouse after 1 month of WD feeding and in all mice after 3 months of WD (figs. S26 and S27). Together with past studies using this high-fat, high-fructose model (42, 43), these results suggest that the mice were in the early stages of progression through the NAFLD/NASH spectrum at the time of the experiments.

KC endolysosomal lipid accumulation in SC and WD mice was assessed in vivo, 24 hours after reporter injection. Results showed that the emission center wavelength of the reporter decreased monotonically with longer periods of WD feeding, indicating an increase in KC endolysosomal lipid accumulation at more advanced stages of NAFLD (Fig. 5C and fig. S28). These results were confirmed via ex vivo measurements of excised livers (Fig. 5D). Analysis of the spectral full width at half maximum (FWHM) of the emission, measured in vivo, showed that they were unchanged in mice at early stages of WD feeding, but they decreased in mice fed the WD for 3 months. Moreover, correlation analysis of spectra center wavelength versus FWHM indicated a minor positive correlation (r = 0.5304; fig. S29). As individual SWCNTs exhibit their own distinct emission spectra, the bulk emission spectrum measured in vivo represents a convolution of spectra from individual nanotubes inside the endolysosomal organelles of hepatic macrophages (fig. S29). Thus, analysis of spectral FWHMs suggests that the observed blue shift was a result of increased lipid accumulation in each KC, rather than simply an increase in the number of KCs harboring lipids, because the latter condition would be expected to cause a broadening of the spectra, a negative correlation coefficient, and an increase in FWHM (fig. S29). Inspection of hepatic tissue from mice on the WD for 3 months via NIR hyperspectral microscopy showed that the reporter was distributed throughout the liver tissue, including in the vicinity of lipogranulomas (fig. S30).

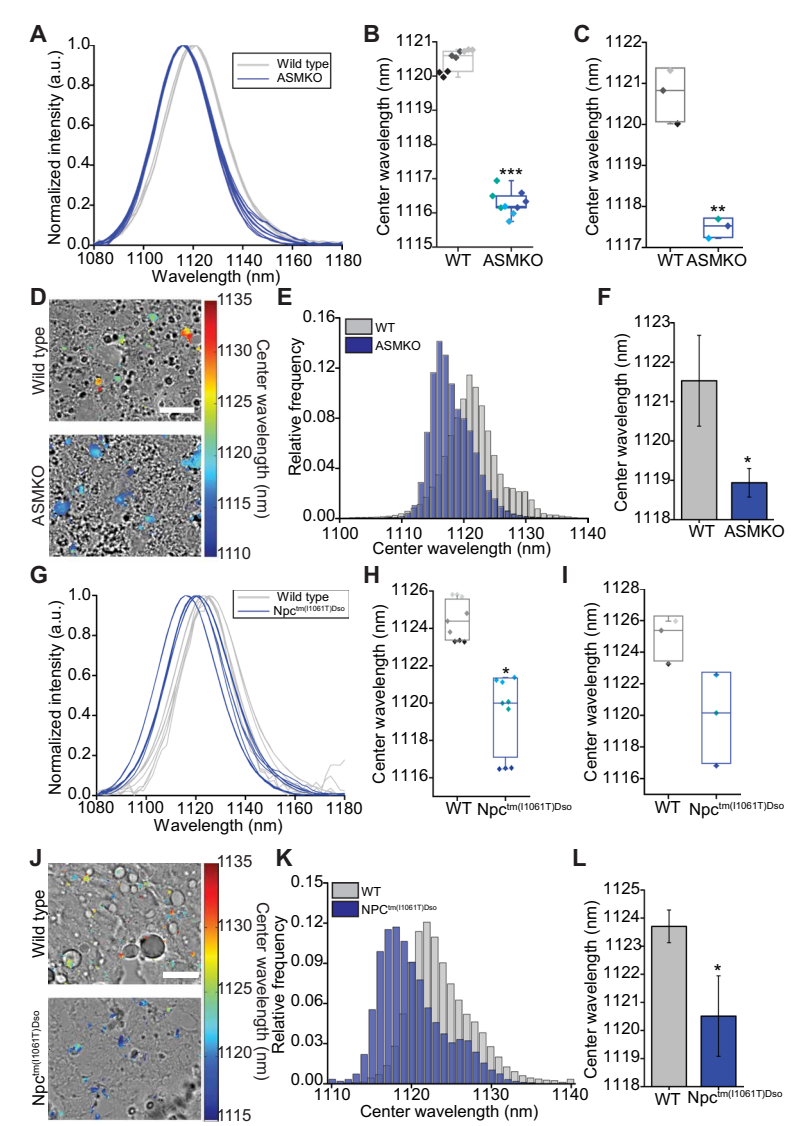


Fig. 3. Noninvasive detection of lysosomal storage disorders in vivo. (A) In vivo emission spectra of the reporter from live wild-type (WT) and ASMKO mice. (B) Box plot of reporter center wavelength from spectra shown in (A). Individual data points are overlaid with diamonds of the same color, indicating repeated spectra taken from a single mouse. (C) Box plot of reporter center wavelength from the livers of WT and ASMKO mice ex vivo. Individual data points are overlaid, with each point representing a different mouse. (D) Overlay of transmitted light and NIR hyperspectral image of nanotube complexes in resected sections of frozen liver tissue from WT and ASMKO mice. Scale bar, 20 um. (E) Histogram of emission center wavelengths of all pixels from NIR hyperspectral images of frozen sections of resected liver tissue from WT and ASMKO mice. (F) Mean center wavelength of reporter emission from frozen sections of resected liver tissue imaged with NIR hyperspectral microscopy. Error bars represent SD. (G) In vivo emission spectra of the reporter from live WT and Npc^{tm(I1061T)Dso} mice. (H) Box plot of reporter center wavelength from spectra shown in (G). Individual data points are overlaid with diamonds of the same color, indicating repeated spectra taken from a single mouse. (I) Box plot of reporter center wavelength from the livers of WT and Npc^{tm(|1061T)Dso} mice ex vivo. Individual data points are overlaid, with each point representing a different mouse. (J) Overlay of transmitted light and NIR hyperspectral image of nanotube complexes in resected sections of frozen liver tissue from WT and Npc^{tm(11061T)Dso} mice. Scale bar, 20 μm. (**K**) Histogram of emission center wavelengths of all pixels from NIR hyperspectral images of frozen sections of resected liver tissue from WT and Npc^{tm(|1061T)Dso} mice. (L) Mean center wavelength of reporter emission taken from frozen sections of resected liver tissue with NIR hyperspectral microscopy. Error bars represent SD. *P < 0.05, **P < 0.01, ***P < 0.001, t test with Welch's correction. n = 3 mice per group.

Effects of the reporter on liver histology and blood chemistry

To assess the effect of the reporter on the livers of SC and WD mice, a trained pathologist analyzed H&E-stained liver sections of reporter-injected and control mice. Sections showed that the reporter did not alter the liver pathology of mice fed SC or WD for 3 months (fig. S27). To further assess the effect of the reporter on mice fed SC or WD for 3 months, we injected mice with the reporter and performed serum chemistry measurements 24 hours thereafter. Between injected and control mice fed SC, no substantial differences were found for the liver injury markers alanine aminotransferase (ALT), aspartate aminotransferase (AST), AST/ALT, lactate dehydrogenase (LDH), alkaline phosphatase (ALP), globulin (GLOB), or albumin (ALB)/GLOB (fig. S31). Although ALB and total protein concentrations were slightly different, to a statistically significant degree (P < 0.05), between control and injected SC mice, the concentrations in the injected mice were actually slightly increased compared to control mice (low concentrations of ALB and total protein may be indicative of liver dysfunction).

Serum chemistry measurements in mice fed the WD for 3 months showed little difference in the levels of AST, AST/ALT, ALB, GLOB, ALB/GLOB, or total protein between control and reporter-injected mice. Although differences were seen in the concentrations of ALT, LDH, and ALP between control and injected mice, these differences would suggest increased liver injury in control, rather than injected, mice. These differences are most likely related to the increased weight of mice from the uninjected control group (fig. S31). The data suggest that this weight disparity between the two groups was random, because mice were placed into groups randomly and measuring the weights of vehicle (PBS)- or reporter-injected mice before, and 24 hours after, injection (to mimic experimental conditions) showed no differences in weight change between the two groups (fig. S32).

To determine whether the reporter dampened the inflammatory response and thus hepatocyte injury, we induced hepatic injury in mice via intraperitoneal administration of lipopolysaccharide (LPS) after intravenous injection of the reporter or vehicle control. Serum quantities of ALT, a serum marker specific for liver injury, were increased, indicating that hepatic injury had been induced by LPS (fig. S32); however, we found little change in amounts of ALT between reporter- and vehicle-injected mice after LPS administration, suggesting that the extent of injury was not substantially altered because of the presence of the reporter (fig. S32). Furthermore, LDH and ALP serum concentrations, two markers that may be indicative of hepatic injury but are less specific than ALT, were also similar in reporter- and vehicle-injected mice, further suggesting that the reporter did not dampen the KC inflammatory response (fig. S32).

Hepatic gene expression after reporter injection

The effect of the reporter on innate immune system activation was investigated by injecting mice with the reporter or PBS as a control. Hepatic expression of $Ifn\alpha$, $Ifn\beta 1$, Il-6,

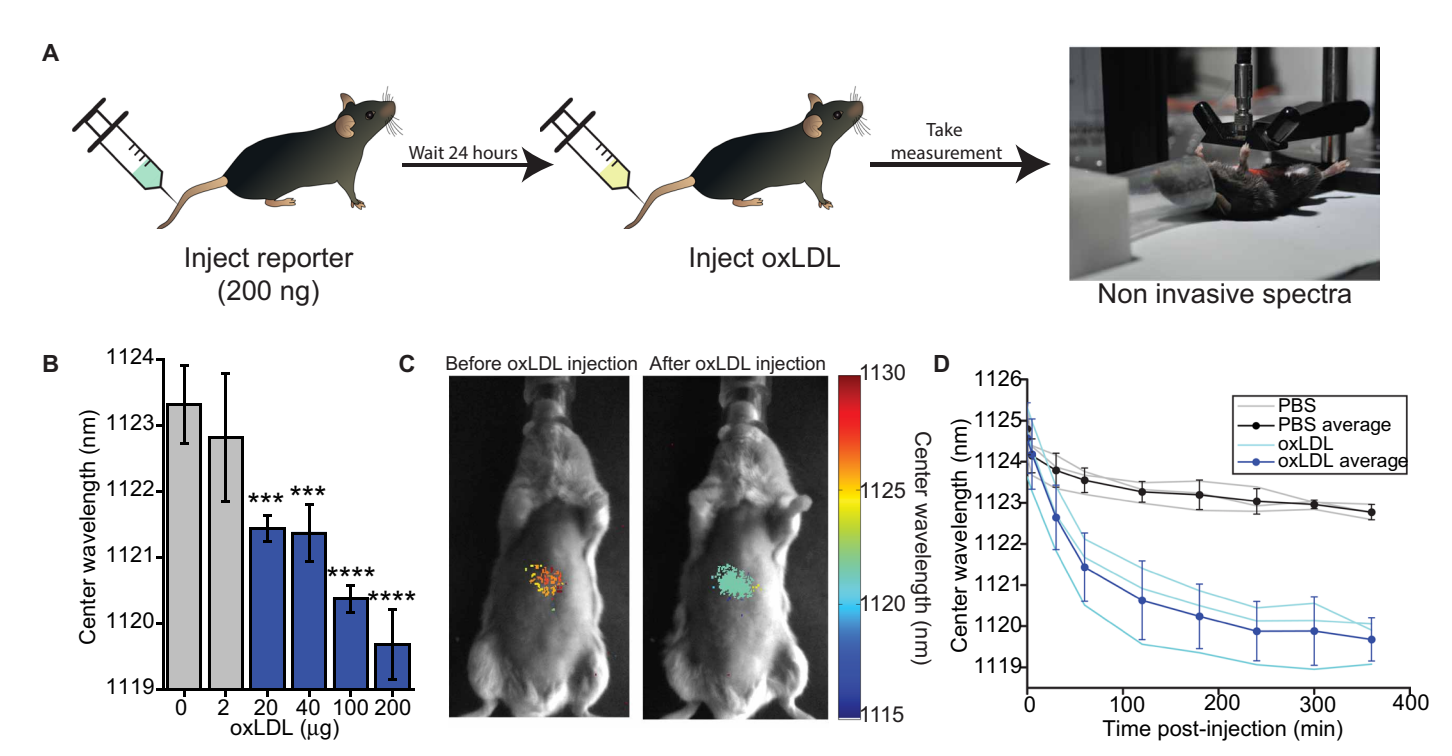


Fig. 4. Dynamic detection of oxLDL accumulation. (**A**) Schematic of experimental procedure used in (B) to (D), shown with a photograph of the NIR in vivo spectroscope (right) used for data acquisition. (**B**) Mean center wavelength of reporter emission from C57BL/6 mice injected with oxLDL. Error bars represent SD. (**C**) Overlay of transmitted light and NIR hyperspectral image of reporter emission in vivo before and after oxLDL injection in mice. (**D**) Trajectories of endolysosomal lipid accumulation from mice injected with oxLDL (200 μ g) or phosphate-buffered saline (PBS). Error bars represent SD. ***P < 0.001, ****P < 0.0001 compared to control, one-way ANOVA with Dunnett's post-test. *n* = 3 mice per experimental group and *n* = 8 mice for control mice injected with PBS (0 μ g of oxLDL).

Il-10, Il-28a, Il-28b, Il-29, Il-8, Tnf α , *Tgf* β 1, *Cxcl10*, and *Isg15* was not substantially altered after reporter injection, suggesting that this does not lead to activation of the innate immune system (fig. S33).

Long-term effects of WD feeding on KC endolysosomal lipids

Mice were given the WD and HFCS for 2 weeks to investigate the long-term effects of these dietary changes. Reporter measurements indicated that this time period was sufficient to induce KC endolysosomal lipid accumulation (Fig. 5E), whereas histological sections confirmed the presence of lipid accumulation in hepatocytes and KCs (figs. S34 to S37). Separate groups of mice were then taken off of the WD and fed SC for two or six additional weeks. Reporter measurements indicated that switching from WD to SC feeding, even for a time period of 6 weeks, resulted in only partial reversal of KC endolysosomal lipid accumulation (Fig. 5E). In contrast, histopathologic analysis reveals complete reversal of steatosis and inflammatory changes even within 2 weeks (fig. S38). This suggests that a high-fat, high-fructose diet may have long-lasting implications on KC physiology that can be detected with the reporter but not with currently available histopathologic techniques.

Longitudinal detection of KC endolysosomal lipid accumulation

The ability of the reporter to detect endolysosomal lipid accumulation over time in the same mice was tested by injecting C57BL/6 mice with reporter intravenously and measuring the emission wavelength 24 hours later (day 0). Mice were then fed either SC or WD with HFCS for 2 weeks. After 2 weeks, a NIR spectroscope was used

on the live mice to verify that signal could not be detected from the first injection of the reporter (mice where signal was noticeable were excluded from further analysis) before mice were injected with a second dose of the reporter (100 ng), and reporter emission wavelength was measured 24 hours later (day 15). Results showed that reporter emission in mice had blue-shifted over time but that the magnitude of this blue shifting was significantly greater (P = 0.001) in mice fed the WD for the 2-week period (Fig. 5F). These results validate the potential of the reporter for use in long-term, longitudinal studies, an application with the ability to greatly increase the efficiency and affordability of the drug development process.

DISCUSSION

Here, we present a method for the noninvasive detection of endoly-sosomal lipid accumulation in vivo. Central to this method was the development of a nanoreporter consisting of the (9,4) SWCNT non-covalently complexed with the single-stranded oligonucleotide CTTC₃TTC. When injected intravenously, the reporter accumulated in the liver and localized specifically within KCs, consistent with multiple studies performed using polymer-wrapped SWCNTs and other classes of non-PEGylated/passivated nanoparticles that can be opsonized within the bloodstream (32–35). Serum measurements of liver health markers and examination of histological tissue sections suggest that the reporter does not cause or enhance hepatic inflammation or injury in healthy or steatotic livers, in agreement with previous studies showing that carbon nanotube reporters composed of relatively short SWCNTs noncovalently functionalized

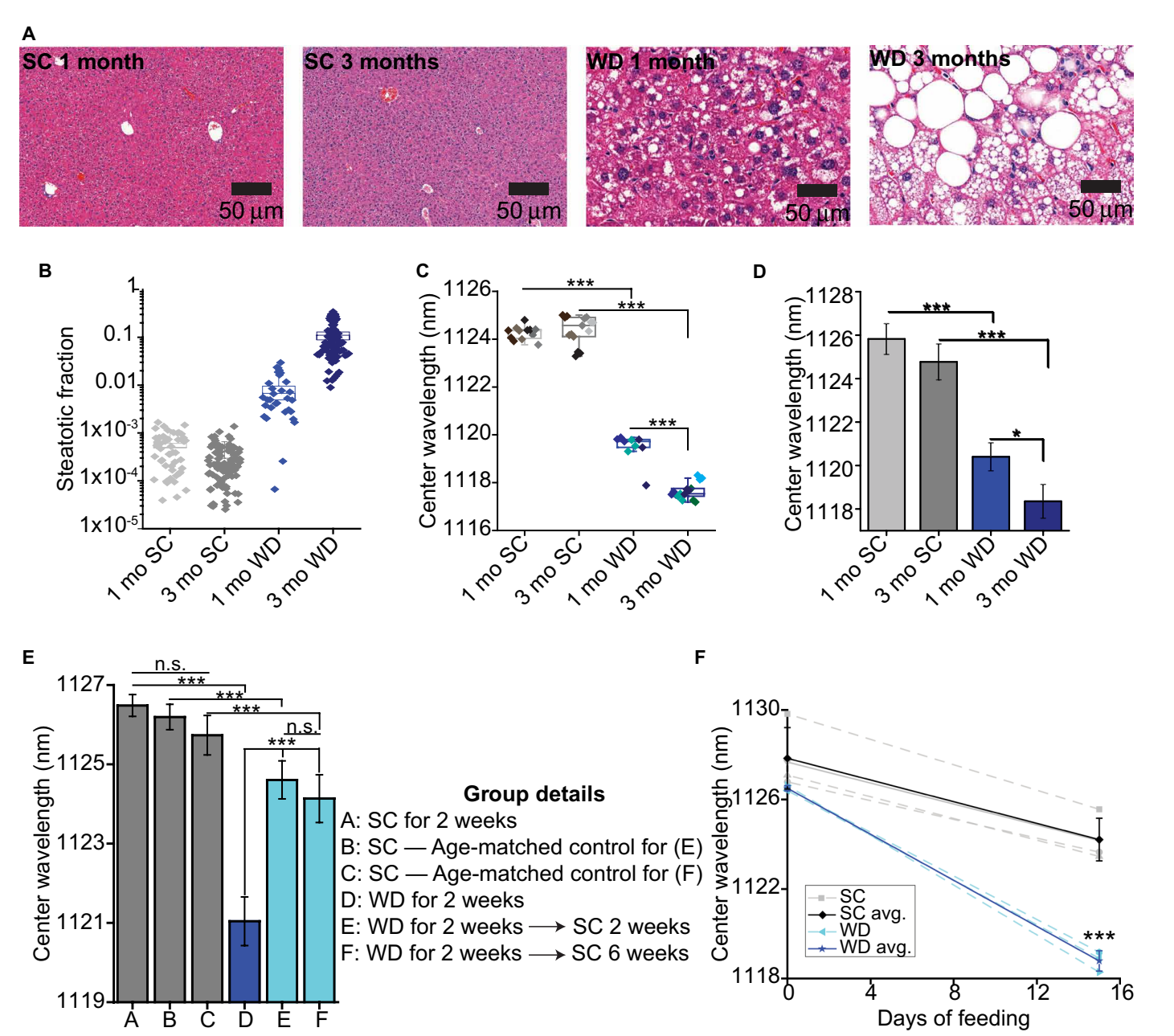


Fig. 5. Measurement of KC endolysosomal lipid flux in a NAFLD model. (A) H&E-stained liver tissue from C57BL/6 mice fed either the WD or SC for 1 or 3 months. (B) Quantification of steatotic area observed in H&E sections from SC or WD mice. Ten to 20 sections were observed per mouse for a total of 30 to 100 sections per group. (C) Box plots of reporter center wavelengths of in vivo emission spectra of the reporter from WD- or SC-fed mice. Individual data points are overlaid with diamonds of the same color, indicating repeated spectra taken from a single mouse. (D) Mean center wavelength of reporter emission from the mouse livers in (C) ex vivo. Error bars represent SD. (E) Mean center wavelength of reporter emission from live WD- or SC-fed mice at various time points. Error bars represent SD. n.s., not significant. (F) Reporter center wavelength in live C57BL/6 mice over time with SC or WD feeding. Separate injections of reporter were used to obtain signal on days 0 and 15. Solid lines indicate averages, and error bars represent SD. *P < 0.05, ***P < 0.001, one-way ANOVA with Sidak's post-test (A to E) or a t test with Welch's correction (F). n = 3 to 5 mice per group.

with amphiphilic polymers/oligonucleotides have well-documented biocompatibility in live cells (17, 44) and animals (37, 38).

The reporter measured lipid accumulation specifically within endolysosomal organelles and was applicable to different lipid species. The reporter's response to lipids was assessed against several modified lipids directly in solution, in live cells via treatment with chemical inhibitors that promoted accumulation of different compositions (predominantly cholesterol or sphingomyelin), in well-

established in vivo models of lysosomal storage diseases that also cause accumulation of different lipids, as well as upon intravenous injection of oxLDL.

Potential limitations of this work include questions of lipid type specificity and organ localization of the reporter. The current reporter responds generally to lipid accumulation within endosomes/lysosomes and does not distinguish between distinct lipid species. However, TEM, the current gold standard for the

detection of endolysosomal lipid accumulation in animal models, is also unable to distinguish between distinct lipid species. Moreover, the generality of the reporter suggests applicability to a range of pathologies, which is likely to prove advantageous in the future. Although the present work only demonstrates in vivo detection in the KC endolysosomal organelles of mice, we expect that alternative reporter delivery methods may allow for the interrogation of other cell types. Past work supports this expectation, including work on the lateral ventricular injection of carbon nanotubes (45). Moreover, improvements in spectroscopic equipment, such as an endoscopic probe that can excite the reporter through the stomach lining, may permit the use of the reporter in larger animal models.

On the basis of its effectiveness and biocompatibility, we believe that this reporter can be applicable to several types of studies in multiple disease classes. When testing the efficacy of drugs designed to treat lysosomal storage disorders such as NPC disease, researchers must currently rely on the measurement of indirect biomarkers or methods such as TEM, which require the euthanization of animals. Longitudinal assessment of endolysosomal lipid accumulation using the reporter was possible in vivo upon repeated administrations in the same mice over both the short and long term. Use of the reporter in this scenario could improve the speed and reduce animal numbers in certain drug development investigations.

The reporter could also be useful in the development of antibiotic, antidepressant, antipsychotic, antimalarial, and antiarrhythmic drugs, because drugs of these classes often have the side effect of DIPL, which may delay the regulatory process. Companies such as Pfizer (12) and Bristol-Meyers Squibb (4) have developed risk management strategies to apply to DIPL during the drug development process; however, these strategies rely on indirect biomarkers or TEM to assess the presence of DIPL in vivo (46), hindering the development of new drugs. We expect that the rapid nature of the method described here will allow for the aforementioned risk management strategies to be streamlined, enabling a more efficient and cost-effective drug development process.

In addition to improving the drug development process, the nanoreporter will also enable new research into the mechanisms linking endolysosomal lipid accumulation and the progression of various diseases such as NAFLD. Here, we examined the relationship between KC endolysosomal lipid accumulation and NAFLD progression, observing an increase in KC endolysosomal lipid accumulation as NAFLD progressed toward NASH. Moreover, we found that diet-induced KC endolysosomal lipid accumulation persisted for at least 6 weeks after the cessation of the high-fat, high-fructose diet. Although correlative, these results support the hypotheses that KC endolysosomal lipid accumulation plays a role in NAFLD progression and that even small modifications in diet induce long-term changes in KC physiology that may portend disease advancement toward NASH. Deeper investigations of a potential mechanistic link between KC endolysosomal lipid accumulation and NAFLD progression are warranted. Such studies will aid in the development of NAFLD/NASH therapies and may also potentiate KC endolysosomal lipid accumulation as a biomarker of NAFLD progression that can then be rapidly assessed in preclinical animal models with the reporter.

This work describes a new technology capable of quantitative, rapid, dynamic, and noninvasive detection of endolysosomal lipid accumulation in vivo. This method has advantages over previously used histological techniques and may be broadly applicable for streamlining preclinical drug development processes and enabling new research into the pathogenesis of lipid-linked diseases.

MATERIALS AND METHODS

Study design

This study aimed to develop and apply an in vivo optical reporter for endolysosomal lipid accumulation. We assessed the reporter's function in two different mouse models of lysosomal storage diseases, which are known to accumulate lipids in KC lysosomes. We measured reporter emission wavelength after injection into these models using a custom-built in vivo spectroscope and confirmed the phenotype of mice via traditional histological methods. We applied the reporter to the study of NAFLD by inducing the disease in mice via feeding with a WD and supplementing drinking water with HFCS. Control mice were fed SC. We assessed disease state via quantification of lipid droplets in hepatic sections and analysis of tissue sections by a trained pathologist. Diets, as well as nanotube or vehicle injections for safety studies, were randomly allocated to mice. Experimental and control groups were age-matched for all studies

Because of obvious differences in the physical appearance of WD-fed and lysosomal storage disease–afflicted mice, complete blinding of experiments was not possible. When assessing histological sections for the effect of the reporter on liver pathology, the trained pathologist analyzing samples was blinded to the injection of nanotubes or vehicle control in specified samples. Details on experimental replicates are provided in the relevant figure legends. Sample sizes were determined on the basis of the authors' previous experiences with experimental equipment that show minimal instrumental noise.

Animal studies

All animal studies were approved by and carried out in accordance with the Memorial Sloan Kettering Cancer Center Institutional Animal Care and Use Committee. Male C57BL/6 mice were purchased from the Jackson Laboratory at 4 to 8 weeks of age. For observing ssCTTC₃TTC-SWCNT removal from blood, 6-week-old male SKH1-Elite mice were purchased from Charles River Laboratories. Mice for the ASMKO experiment were provided by the Schuchman laboratory (39) and used at 5 months of age. NPC1 I1061T and wildtype controls were bred in the laboratory of D.S.O., and experiments were performed when mice were 13 weeks of age. All control and experimental mice were age-matched and housed in identical environments. For longitudinal in vivo sensing experiments, mice were injected in the tail vein with 200 μl of ssCTTC₃TTC-(9,4) (0.5 mg/liter) diluted in PBS. For all other in vivo sensing experiments, a dose of 200 µl of ssCTTC₃TTC-(9,4) (1.0 mg/liter) was used. For the hepatic cell isolation experiments, unsorted ssCTTC₃TTC eg150X SWCNT (18 mg/liter) was injected. For in vivo imaging and spectroscopy, mice were anesthetized with 2% isoflurane before data collection.

Statistical analysis

GraphPad Prism versions 6.02 and 7 were used to perform statistical analysis. All data met the assumptions of the statistical tests performed (normality, equal variances), and two-sided testing was performed in all instances. The F test and Brown-Forsythe tests were used to determine whether variance was similar between groups for t tests and for one-way ANOVAs, respectively, to ensure that the assumptions of tests were met. The testing of multiple hypotheses was accounted for by performing one-way ANOVAs with Dunnett's, Tukey's, or Sidak's post-tests when appropriate. Information on specific statistical tests performed can be found in the figure legends. P < 0.05 was deemed significant.

SCIENCE TRANSLATIONAL MEDICINE | RESEARCH ARTICLE

SUPPLEMENTARY MATERIALS

www.sciencetranslationalmedicine.org/cgi/content/full/10/461/eaar2680/DC1 Materials and Methods

- Fig. S1. Two-dimensional photoluminescence plots of isolated SWCNT chiralities.
- Fig. S2. Identification of ssCTTC₃TTC-(9,4) as a potential probe for endolysosomal lipid
- Fig. S3. Representative emission spectra of ssCTTC₃TTC-(9,4) at a neutral and acidic pH.
- Fig. S4. ssCTTC₃TTC-(9,4) photoluminescent response in solution.
- Fig. S5. Atomic force microscopy of ssCTTC₃TTC-(9.4) complexes.
- Fig. S6. Initial REMD configurations.
- Fig. S7. Analysis of REMD simulations.
- Fig. S8. Mean emission wavelength of ssCTTC₃TTC-(9,4) in live RAW 264.7 macrophages treated with inhibitors.
- Fig. S9. Effect of inhibitors on ssCTTC₃TTC-(9,4) emission spectra in solution.
- Fig. S10. Reporter response to HPβCD treatment in MEFs.
- Fig. S11. Assessing the effect of ssCTTC₃TTC-(9,4) on lipoprotein hydrolysis.
- Fig. S12. NIR in vivo spectroscope.
- Fig. S13. Representative images of liver tissue from wild-type and ASMKO mice.
- Fig. S14. Representative images of hepatic tissues from wild-type and ASMKO mice stained with the hepatocyte marker CK8/18.
- Fig. S15. Representative images of hepatic tissue from wild-type and ASMKO mice stained with the KC marker F4/80.
- Fig. S16. Representative images from H&E-stained tissues from the livers of wild-type and Npc^{tm(I1061T)Dso} mice.
- Fig. S17. Representative images of hepatic tissue from wild-type and $Npc^{tm(11061T)Dso}$ mice stained with the hepatocyte marker CK8/18.
- Fig. S18. Representative images of hepatic tissues from wild-type and $\mathrm{Npc}^{\mathrm{tm}(1061T)\mathrm{Dso}}$ mice stained with the KC marker F4/80.
- Fig. S19. Exponential fits of the decrease in ssCTTC₃TTC-(9,4) emission wavelength after intravenous injection of 200 µg of oxLDL in mice.
- Fig. S20. Testing the effects of elevated lipid concentrations on reporter emission in whole blood. Fig. S21. Weights of male C57BL/6 mice fed SC or WD with HFCS.
- Fig. S22. Representative images of hepatic tissues stained with CK8/18 from mice fed SC or WD with HFCS for 1 month
- Fig. S23. Representative images of hepatic tissues stained with F4/80 from mice fed SC or WD with HFCS for 1 month.
- Fig. S24. Representative images of hepatic tissues stained with CK8/18 from mice fed SC or WD with HFCS for 3 months
- Fig. S25. Representative images of hepatic tissues stained with F4/80 from mice fed SC or WD with HFCS for 3 months.
- Fig. S26, Representative images of H&E-stained liver tissues from C57BL/6 mice fed SC or WD with HFCS for 1 month.
- Fig. S27. Representative H&E-stained liver tissues from mice fed SC or WD with HFCS for 3 months. Fig. S28. In vivo emission spectra of the reporter from the liver of mice fed SC or WD with HFCS for 1 to 3 months.
- Fig. S29. Analysis of intercellular heterogeneity of KC lipid content in vivo.
- Fig. S30. Reporter presence in relation to lipogranulomas.
- Fig. S31. Weight and serum chemistry measurements of mice fed SC or WD with HFCS for 3 months. Fig. S32. Serum chemistry measurements and weights of reporter- and vehicle-injected mice in a model of hepatic injury.
- Fig. S33. Relative hepatic expression of genes involved in the innate immune response after injection with ssCTTC₃TTC-(9,4) or PBS.
- Fig. S34. Representative images of H&E-stained liver tissue from C57BL/6 mice fed SC or WD
- Fig. S35. Representative images of liver tissue stained with Oil Red O neutral lipid stain. Fig. S36. Representative images of hepatic tissue from mice fed SC or WD with HFCS for
- 2 weeks stained with the hepatocyte marker CK8/18. Fig. S37. Representative images of hepatic tissue from mice fed SC or WD with HFCS for 2 weeks stained with the KC marker F4/80.
- Fig. S38. Representative H&E sections of livers from mice shown in Fig. 5E.
- Table S1. Average reporter emission center wavelengths measured from wild-type and ASMKO mice in vivo, ex vivo, and in frozen sections of resected liver tissue.
- Table S2. Average reporter emission center wavelengths measured from wild-type and $\label{eq:potential} Npc^{tm(1061T)Dso}\stackrel{-}{\text{mice in vivo, ex vivo, and in frozen sections of resected liver tissue.}}$
- Table S3. Individual mouse data.
- References (47-56)

REFERENCES AND NOTES

- 1. R. A. Nixon, The role of autophagy in neurodegenerative disease. Nat. Med. 19, 983–997 (2013).
- 2. A. H. Futerman, G. van Meer, The cell biology of lysosomal storage disorders. Nat. Rev. Mol. Cell Biol. 5, 554-565 (2004).

- 3. T. Hendrikx, S. M. A. Walenbergh, M. H. Hofker, R. Shiri-Sverdlov, Lysosomal cholesterol accumulation: Driver on the road to inflammation during atherosclerosis and non-alcoholic steatohepatitis. Obes. Rev. 15, 424-433 (2014).
- 4. L. LeCureux, C. S. Cheng, J. Herbst, T. P. Reilly, L. Lehman-McKeeman, M. Otieno, Evaluation and validation of multiple cell lines and primary mouse macrophages to predict phospholipidosis potential. Toxicol. In Vitro 25, 1934-1943 (2011).
- 5. S. B. Heymsfield, H. H. Hu, W. Shen, O. Carmichael, Emerging technologies and their applications in lipid compartment measurement. Trends Endocrinol. Metab. 26, 688-698
- 6. T. Kubo, A. Tanaka, Y. Ino, H. Kitabata, Y. Shiono, T. Akasaka, Assessment of coronary atherosclerosis using optical coherence tomography. J. Atheroscler. Thromb. 21, 895–903
- 7. M. Jaguszewski, R. Klingenberg, U. Landmesser, Intracoronary near-infrared spectroscopy (NIRS) imaging for detection of lipid content of coronary plagues: Current experience and future perspectives. Curr. Cardiovasc. Imaging Rep. 6, 426-430 (2013).
- 8. T. A. Kuemmel, J. Thiele, R. Schroeder, W. Stoffel, Pathology of visceral organs and bone marrow in an acid sphingomyelinase deficient knock-out mouse line, mimicking human Niemann-Pick disease type A: A light and electron microscopic study. Pathol. Res. Pract. 193, 663-671 (1997).
- 9. A. M. Schrand, J. J. Schlager, L. Dai, S. M. Hussain, Preparation of cells for assessing ultrastructural localization of nanoparticles with transmission electron microscopy. Nat. Protoc. 5, 744-757 (2010).
- 10. N. Liu, E. A. Tengstrand, L. Chourb, F. Y. Hsieh, Di-22:6-bis (monoacylglycerol) phosphate: A clinical biomarker of drug-induced phospholipidosis for drug development and safety assessment. Toxicol. Appl. Pharmacol. 279, 467-476 (2014).
- 11. B. R. Berridge, L. A. Chatman, M. Odin, A. E. Schultze, P. E. Losco, J. T. Meehan, T. Peters, S. L. Vonderfecht; Society of Toxicologic Pathology Scientific and Regulatory Policy Committee Working Group, Phospholipidosis in nonclinical toxicity studies. Toxicol. Pathol. 35, 325 (2007).
- L. A. Chatman, D. Morton, T. O. Johnson, S. D. Anway, A strategy for risk management of drug-induced phospholipidosis. Toxicol. Pathol. 37, 997-1005 (2009)
- 13. G. Musso, R. Gambino, M. Cassader, Cholesterol metabolism and the pathogenesis of non-alcoholic steatohepatitis. Prog. Lipid Res. 52, 175-191 (2013).
- 14. V. Bieghs, F. Verheyen, P. J. van Gorp, T. Hendrikx, K. Wouters, D. Lütjohann, M. J. J. Gijbels, M. Febbraio, C. J. Binder, M. H. Hofker, R. Shiri-Sverdlov, Internalization of modified lipids by CD36 and SR-A leads to hepatic inflammation and lysosomal cholesterol storage in Kupffer cells. PLOS ONE 7, e34378 (2012).
- 15. V. Bieghs, S. M. A. Walenbergh, T. Hendrikx, P. J. van Gorp, F. Verheyen, S. W. Olde Damink, A. A. Masclee, G. H. Koek, M. H. Hofker, C. J. Binder, R. Shiri-Sverdlov, Trapping of oxidized LDL in lysosomes of Kupffer cells is a trigger for hepatic inflammation. Liver Int. 33, 1056-1061 (2013).
- 16. S. Parekh, F. A. Anania, Abnormal lipid and glucose metabolism in obesity: Implications for nonalcoholic fatty liver disease. Gastroenterology 132, 2191-2207
- 17. P. V. Jena, D. Roxbury, T. V. Galassi, L. Akkari, C. P. Horoszko, D. B. laea, J. Budhathoki-Uprety, N. Pipalia, A. S. Haka, J. D. Harvey, J. Mittal, F. R. Maxfield, J. A. Joyce, D. A. Heller, A carbon nanotube optical reporter maps endolysosomal lipid flux. ACS Nano 11, 10689-10703 (2017).
- 18. S. M. Bachilo, M. S. Strano, C. Kittrell, R. H. Hauge, R. E. Smalley, R. B. Weisman, Structure-assigned optical spectra of single-walled carbon nanotubes. Science 298, 2361-2366 (2002).
- 19. M. J. O'Connell, S. M. Bachilo, C. B. Huffman, V. C. Moore, M. S. Strano, E. H. Haroz, K. L. Rialon, P. J. Boul, W. H. Noon, C. Kittrell, J. Ma. R. H. Hauge, R. B. Weisman, R. E. Smalley, Band gap fluorescence from individual single-walled carbon nanotubes. Science 297, 593-596 (2002).
- 20. G. Ao, J. K. Streit, J. A. Fagan, M. Zheng, Differentiating left-and right-handed carbon nanotubes by DNA. J. Am. Chem. Soc. 138, 16677-16685 (2016).
- 21. X. Tu, S. Manohar, A. Jagota, M. Zheng, DNA sequence motifs for structure-specific recognition and separation of carbon nanotubes. Nature 460, 250-253 (2009).
- 22. G. Ao, C. Y. Khripin, M. Zheng, DNA-controlled partition of carbon nanotubes in polymer aqueous two-phase systems. J. Am. Chem. Soc. 136, 10383-10392 (2014).
- 23. C.-L. Tsai, J.-C. Chen, W.-J. Wang, Near-infrared absorption property of biological soft tissue constituents. J. Med. Biol. Eng. 21, 7-14 (2001).
- 24. C.-W. Lin, S. M. Bachilo, M. Vu, K. M. Beckingham, R. B. Weisman, Spectral triangulation: A 3D method for locating single-walled carbon nanotubes in vivo. Nanoscale 8, 10348-10357 (2016).
- 25. F. Lu, Q. Liang, L. Abi-Mosleh, A. Das, J. K. De Brabander, J. L. Goldstein, M. S. Brown, Identification of NPC1 as the target of U18666A, an inhibitor of lysosomal cholesterol export and Ebola infection. eLife 4, e12177 (2015).
- 26. A. I. Rosenbaum, F. R. Maxfield, Niemann-Pick type C disease: Molecular mechanisms and potential therapeutic approaches. J. Neurochem. 116, 789-795 (2011).

SCIENCE TRANSLATIONAL MEDICINE | RESEARCH ARTICLE

- A. I. Rosenbaum, C. C. Cosner, C. J. Mariani, F. R. Maxfield, O. Wiest, P. Helquist, Thiadiazole carbamates: Potent inhibitors of lysosomal acid lipase and potential Niemann–Pick type C disease therapeutics. J. Med. Chem. 53, 5281–5289 (2010).
- H. R. Sloan, D. S. Fredrickson, Enzyme deficiency in cholesteryl ester storage disease.
 J. Clin. Invest. 51, 1923–1926 (1972).
- N. Beckmann, D. Sharma, E. Gulbins, K. A. Becker, B. Edelmann, Inhibition of acid sphingomyelinase by tricyclic antidepressants and analogons. Front. Physiol. 5, 331 (2014).
- D. Roxbury, P. V. Jena, R. M. Williams, B. Enyedi, P. Niethammer, S. Marcet, M. Verhaegen,
 Blais-Ouellette, D. A. Heller, Hyperspectral microscopy of near-infrared fluorescence enables 17-chirality carbon nanotube imaging. Sci. Rep. 5, 14167 (2015).
- A. I. Rosenbaum, G. Zhang, J. D. Warren, F. R. Maxfield, Endocytosis of beta-cyclodextrins is responsible for cholesterol reduction in Niemann-Pick type C mutant cells. *Proc. Natl. Acad. Sci. U.S.A.* 107, 5477–5482 (2010).
- R. Gref, A. Domb, P. Quellec, T. Blunk, R. H. Müller, J. M. Verbavatz, R. Langer, The controlled intravenous delivery of drugs using PEG-coated sterically stabilized nanospheres. *Adv. Drug Deliv. Rev.* 64, 316–326 (2012).
- L. Illum, S. Davis, R. Müller, E. Mak, P. West, The organ distribution and circulation time of intravenously injected colloidal carriers sterically stabilized with a blockcopolymer– poloxamine 908. Life Sci. 40, 367–374 (1987).
- D. E. Owens III, N. A. Peppas, Opsonization, biodistribution, and pharmacokinetics of polymeric nanoparticles. *Int. J. Pharm.* 307, 93–102 (2006).
- R. Gref, Y. Minamitake, M. T. Peracchia, V. Trubetskoy, V. Torchilin, R. Langer, Biodegradable long-circulating polymeric nanospheres. Science 263, 1600–1603 (1994).
- Z. Liu, C. Davis, W. Cai, L. He, X. Chen, H. Dai, Circulation and long-term fate of functionalized, biocompatible single-walled carbon nanotubes in mice probed by Raman spectroscopy. *Proc. Natl. Acad. Sci. U.S.A.* 105, 1410–1415 (2008).
- M. L. Schipper, N. Nakayama-Ratchford, C. R. Davis, N. W. S. Kam, P. Chu, Z. Liu, X. Sun, H. Dai, S. S. Gambhir, A pilot toxicology study of single-walled carbon nanotubes in a small sample of mice. *Nat. Nanotechnol.* 3, 216–221 (2008).
- N. M. Iverson, P. W. Barone, M. Shandell, L. J. Trudel, S. Sen, F. Sen, V. Ivanov, E. Atolia, E. Farias, T. P. McNicholas, N. Reuel, N. M. A. Parry, G. N. Wogan, M. S. Strano, In vivo biosensing via tissue-localizable near-infrared-fluorescent single-walled carbon nanotubes. *Nat. Nanotechnol.* 8, 873–880 (2013).
- K. Horinouchil, S. Erlichl, D. P. Perlz, K. Ferlinz, C. L. Bisgaier, K. Sandhoff, R. J. Desnick,
 C. L. Stewart, E. H. Schuchman, Acid sphingomyelinase deficient mice: A model of types A and B Niemann–Pick disease. *Nat. Genet.* 10, 288–293 (1995).
- M. Praggastis, B. Tortelli, J. Zhang, H. Fujiwara, R. Sidhu, A. Chacko, Z. Chen, C. Chung, A. P. Lieberman, J. Sikora, C. Davidson, S. U. Walkley, N. H. Pipalia, F. R. Maxfield, J. E. Schaffer, D. S. Ory, A murine Niemann-Pick C1 I1061T knock-in model recapitulates the pathological features of the most prevalent human disease allele. *J. Neurosci.* 35, 8091–8106 (2015).
- J. D. Harvey, P. V. Jena, H. A. Baker, G. H. Zerze, R. M. Williams, T. V. Galassi, D. Roxbury, J. Mittal, D. A. Heller, A carbon nanotube reporter of microRNA hybridization events in vivo. *Nat. Biomed. Eng.* 1, 0041 (2017).
- A. Asgharpour, S. C. Cazanave, T. Pacana, M. Seneshaw, R. Vincent, B. A. Banini, D. P. Kumar, K. Daita, H.-K. Min, F. Mirshahi, P. Bedossa, X. Sun, Y. Hoshida, S. V. Koduru, D. Contaifer Jr., U. O. Warncke, D. S. Wijesinghe, A. J. Sanyal, A diet-induced animal model of non-alcoholic fatty liver disease and hepatocellular cancer. J. Hepatol. 65, 579–588 (2016).
- M. N. VanSaun, I. K. Lee, M. K. Washington, L. Matrisian, D. L. Gorden, High fat diet induced hepatic steatosis establishes a permissive microenvironment for colorectal metastases and promotes primary dysplasia in a murine model. *Am. J. Pathol.* 175, 355–364 (2009).
- J. Budhathoki-Uprety, R. E. Langenbacher, P. V. Jena, D. Roxbury, D. A. Heller, A carbon nanotube optical sensor reports nuclear entry via a noncanonical pathway. ACS Nano 11, 3875–3882 (2017).
- A. G. Godin, J. A. Varela, Z. Gao, N. Danné, J. P. Dupuis, B. Lounis, L. Groc, L. Cognet, Single-nanotube tracking reveals the nanoscale organization of the extracellular space in the live brain. *Nat. Nanotechnol.* 12, 238–243 (2017).
- E. T. Baronas, J.-W. Lee, C. Alden, F. Y. Hsieh, Biomarkers to monitor drug-induced phospholipidosis. *Toxicol. Appl. Pharmacol.* 218, 72–78 (2007).
- 47. G. Ao, M. Zheng, Preparation and separation of DNA-wrapped carbon nanotubes. *Curr. Protoc. Chem. Biol.* **7**, 43–51 (2015).
- R. M. Williams, C. Lee, T. V. Galassi, J. D. Harvey, R. Leicher, M. Sirenko, M. A. Dorso, J. Shah, N. Olvera, F. Dao, D. A. Levine, D. A. Heller, Noninvasive ovarian cancer biomarker detection via an optical nanosensor implant. *Sci. Adv.* 4, eaaq1090 (2018).
- D. Roxbury, A. Jagota, J. Mittal, Sequence-specific self-stitching motif of short single-stranded DNA on a single-walled carbon nanotube. J. Am. Chem. Soc. 133, 13545–13550 (2011).
- D. Roxbury, J. Mittal, A. Jagota, Molecular-basis of single-walled carbon nanotube recognition by single-stranded DNA. Nano Lett. 12, 1464–1469 (2012).
- Y. Sugita, Y. Okamoto, Replica-exchange molecular dynamics method for protein folding. Chem. Phys. Lett. 314, 141–151 (1999).

- W. L. Jorgensen, J. Chandrasekhar, J. D. Madura, R. W. Impey, M. L. Klein, Comparison of simple potential functions for simulating liquid water. J. Chem. Phys. 79, 926–935 (1983).
- W. Humphrey, A. Dalke, K. Schulten, VMD: Visual molecular dynamics. J. Mol. Graph. 14, 33–38 (1996).
- L. H. Tetri, M. Basaranoglu, E. M. Brunt, L. M. Yerian, B. A. Neuschwander-Tetri, Severe NAFLD with hepatic necroinflammatory changes in mice fed trans fats and a high-fructose corn syrup equivalent. *Am. J. Physiol. Gastrointest. Liver Physiol.* 295, G987–G995 (2008)
- J. Schindelin, I. Arganda-Carreras, E. Frise, V. Kaynig, M. Longair, T. Pietzsch, S. Preibisch,
 C. Rueden, S. Saalfeld, B. Schmid, J.-Y. Tinevez, D. J. White, V. Hartenstein, K. Eliceiri,
 P. Tomancak, A. Cardona, Fiji: An open-source platform for biological-image analysis.
 Nat. Methods 9, 676–682 (2012).
- I. Mederacke, D. H. Dapito, S. Affò, H. Uchinami, R. F. Schwabe, High-yield and high-purity isolation of hepatic stellate cells from normal and fibrotic mouse livers. *Nat. Protoc.* 10, 305–315 (2015).

Acknowledgments: We would like to thank the Schuchman laboratory for providing ASMKO mice; Y. Shamay, R. Williams, J. Harvey, C. Cupo, J. Budhathoki-Uprety, and J. Kubala for helpful discussions; M. Antman-Passig for cell culture assistance; and M. Sirenko for MATLAB code. We also acknowledge the Molecular Cytology Core Facility at Memorial Sloan Kettering Cancer Center and the Electron Microscopy and Histology Core Facility at Weill Cornell Medicine. Funding: This work was supported, in part, by the NIH New Innovator Award (DP2-HD075698); the Cancer Center Support Grant (P30 CA008748); NIHNS081981 (D.S.O.); the NSF CAREER Award (1752506); the Ara Parseghian Medical Research Fund through the Michael, Marcia and Christa Parseghian Endowment for Excellence in Niemann Pick Type C Research; the Honorable Tina Brozman Foundation for Ovarian Cancer Research; the Expect Miracles Foundation—Financial Services Against Cancer; the Anna Fuller Fund; the Louis V. Gerstner Jr. Young Investigator's Fund; the Frank A. Howard Scholars Program; Cycle for Survival; the Alan and Sandra Gerry Metastasis Research Initiative; Mr. William H. Goodwin and Mrs. Alice Goodwin and the Commonwealth Foundation for Cancer Research; the Experimental Therapeutics Center; the Imaging and Radiation Sciences Program; the Pershing Square Sohn Cancer Research Alliance; the Department of Radiation Oncology, Research and Development funds at Memorial Sloan Kettering Cancer Center; and the Center for Molecular Imaging and Nanotechnology of Memorial Sloan Kettering Cancer. Molecular simulation work was performed at Lehigh University and is supported by the U.S. Department of Energy (DOE) Office of Science, Basic Energy Sciences (BES), and Division of Material Sciences and Engineering, under Award DE-SC0013979. Use of the high-performance computing capabilities of the Extreme Science and Engineering Discovery Environment (XSEDE) was supported by the National Science Foundation (NSF) under grant number TG-MCB-120014. This research also used resources of the National Energy Research Scientific Computing Center, a DOE Office of Science User Facility supported by the Office of Science of the U.S. Department of Energy under Contract No. DE-AC02-05CH11231. D.R. was supported by the American Cancer Society Roaring Fork Valley Postdoctoral Fellowship (PF-13-388801-TBG). P.V.J. was supported by an NIH National Cancer Institute T-32 fellowship (2T32CA062948-21), T.V.G. was supported by the Frank Lappin Horsfall Jr. Fellowship, Author contributions: T.V.G., R.E.S., and D.A.H. conceived and wrote the manuscript. T.V.G., P.V.J., J.S., Y.B., A.F., J.P., J.J., D.R., and J.M. performed experiments and/or data analysis. D.S.O., E.M., and A.H.-F. assisted in experiments involving in vivo models of lysosomal storage diseases. M.Z. and G.A. performed nanotube isolations and advised on sensor preparation techniques. All authors provided input and feedback for manuscript preparation. Competing interests: P.V.J. and D.A.H. are cofounders and officers of LipidSense Inc., a company that develops in vivo assessments of lipid accumulation. P.V.J., D.A.H., and D.R. are named on a patent application filed by Memorial Sloan Kettering Cancer Center related to this work (application no. US20170199126A1; title: Composition and method for monitoring lipid). D.A.H. is a cofounder and officer with equity interest in Goldilocks Therapeutics Inc., as well as a member of the scientific advisory board of Oncorus Inc., two companies that are unrelated to this work. P.V.J. has served as a paid consultant for Photon Etc. and as an unpaid consultant for Goldilocks Therapeutics. D.S.O. is employed by Casma Therapeutics and serves as a consultant for Mallinckrodt Pharmaceuticals. Data and materials availability: ASMKO mice were provided by the Schuchman laboratory under a materials transfer agreement. All data associated with this study are present in the paper or the Supplementary Materials. MATLAB code related to this paper may be requested from the authors.

Submitted 19 October 2017 Resubmitted 5 April 2018 Accepted 10 September 2018 Published 3 October 2018 10.1126/scitranslmed.aar2680

Citation: T. V. Galassi, P. V. Jena, J. Shah, G. Ao, E. Molitor, Y. Bram, A. Frankel, J. Park, J. Jessurun, D. S. Ory, A. Haimovitz-Friedman, D. Roxbury, J. Mittal, M. Zheng, R. E. Schwartz, D. A. Heller, An optical nanoreporter of endolysosomal lipid accumulation reveals enduring effects of diet on hepatic macrophages in vivo. *Sci. Transl. Med.* 10, eaar2680 (2018).

Science Translational Medicine

An optical nanoreporter of endolysosomal lipid accumulation reveals enduring effects of diet on hepatic macrophages in vivo

Thomas V. Galassi, Prakrit V. Jena, Janki Shah, Geyou Ao, Elizabeth Molitor, Yaron Bram, Angela Frankel, Jiwoon Park, Jose Jessurun, Daniel S. Ory, Adriana Haimovitz-Friedman, Daniel Roxbury, Jeetain Mittal, Ming Zheng, Robert E. Schwartz and Daniel A. Heller

Sci Transl Med 10, eaar2680. DOI: 10.1126/scitranslmed.aar2680

Enlightening endolysosomal lipids

Lipid accumulation contributes to multiple diseases including atherosclerosis, nonalcoholic fatty liver disease (NAFLD), and lysosomal storage diseases. To noninvasively measure lipids in vivo, Galassi et al. engineered a carbon nanotube optical reporter for endolysosomal organelle uptake. In mouse models of lysosomal storage disease and NAFLD, the nanoreporter's near-infrared fluorescence tracked lipid accumulation within Kupffer cells (liver macrophages) and revealed that switching mice from a high-fat, high-fructose diet to standard chow only partially reversed liver lipid accumulation. This optical imaging agent could help to elucidate mechanisms of lipid accumulation in disease or be useful for drug development testing.

ARTICLE TOOLS http://stm.sciencemag.org/content/10/461/eaar2680

SUPPLEMENTARY http://stm.sciencemag.org/content/suppl/2018/10/01/10.461.eaar2680.DC1

RELATED http://stm.sciencemag.org/content/scitransmed/5/216/216rv4.full

http://stm.sciencemag.org/content/scitransmed/6/260/260fs44.full http://stm.sciencemag.org/content/scitransmed/8/355/355ra118.full http://stm.sciencemag.org/content/scitransmed/8/326/326ra23.full http://stm.sciencemag.org/content/scitransmed/6/258/258ra141.full http://stm.sciencemag.org/content/scitransmed/3/84/84ra45.full

REFERENCES This article cites 56 articles, 7 of which you can access for free

http://stm.sciencemag.org/content/10/461/eaar2680#BIBL

PERMISSIONS http://www.sciencemag.org/help/reprints-and-permissions

Use of this article is subject to the Terms of Service